



Heterogeneous Catalysis Hot Paper

How to cite:

International Edition: doi.org/10.1002/anie.201916032

German Edition: doi.org/10.1002/ange.201916032

Surface Iron Species in Palladium–Iron Intermetallic Nanocrystals that Promote and Stabilize CO₂ Methanation

Laihao Luo⁺, Menglin Wang⁺, Yi Cui, Ziyuan Chen, Jiaxin Wu, Yulu Cao, Jie Luo, Yizhou Dai, Wei-Xue Li, Jun Bao,* and Jie Zeng*

Abstract: It is of pivotal importance to develop efficient catalysts and investigate the intrinsic mechanism for CO₂ methanation. Now, it is reported that PdFe intermetallic nanocrystals afforded high activity and stability for CO₂ methanation. The mass activity of *fcc*-PdFe nanocrystals reached 5.3 mmol g⁻¹ h⁻¹, under 1 bar (CO₂:H₂=1:4) at 180°C, being 6.6, 1.6, 3.3, and 5.3 times as high as that of *fcc*-PdFe nanocrystals, Ru/C, Ni/C, and Pd/C, respectively. After 20 rounds of successive reaction, 98% of the original activity was retained for PdFe intermetallic nanocrystals. Further mechanistic studies revealed that PdFe intermetallic nanocrystals enabled the maintenance of metallic Fe species via a reversible oxidation–reduction process in CO₂ methanation. The metallic Fe in PdFe intermetallic nanocrystals induced the direct conversion of CO₂ into CO* as the intermediate, contributing to the enhanced activity.

Introduction

Excessive emission of CO₂ has caused a severe impact on the climate.^[1,2] The development of effective ways for the reclamation of CO₂ is gaining increasing interest.^[3–5] One attractive route is CO₂ methanation, which shows great potential in environmental remediation and renewable energy storage.^[6,7] Generally, CO₂ methanation experiences a Langmuir–Hinshelwood-type mechanism.^[8] Specifically, CO₂ dissociates into CO* by a reverse water-gas shift reaction. Afterwards, CO* is directly hydrogenated into methane or dissociates into C* for further hydrogenation. During the methanation process, surface O* is produced either by CO* formation or further CO* dissociation, leading to the oxidation of the catalyst surface. Such oxidation changes the electronic structures of the surface, thereby

influencing the activity and selectivity towards CO₂ methanation. In this case, an optimal catalyst should enable the reduction of the oxidized surface under the reaction condition of CO₂ methanation, thus maintaining a dynamically stable surface.

Noble metals such as Ru and Rh have exhibited remarkable catalytic performance in CO₂ methanation, but suffer from their low abundance and high cost.^[9,10] Alloying noble metals with non-noble ones can not only reduce the material cost, but also efficiently improve the catalytic performance because of the ensemble effect and ligand effect.^[11–13] Specially, the ensemble effect refers to that alloying induces the formation of new geometries of active sites. The ligand effect refers to that alloying alters the electronic properties of the active sites via electron transfer between different metals. Non-noble metals are vulnerable to the oxidation and leaching in harsh chemical environments, resulting in the degradation of the alloys and deterioration of the catalytic stability.^[14,15] A pivotal strategy to enhance the catalytic stability is to arrange the atomic distribution of the alloys in a highly ordered form, in other words constructing intermetallics.^[16,17] For instance, owing to the relatively high segregation energy for both components, Pd and In atoms in PdIn intermetallics revealed enhanced resistance against leaching in CO₂ hydrogenation.^[18] The ordered bonding between Ni and Ga in the Ni₅Ga₃ intermetallic strongly suppressed the segregation, accounting for the long-term stability in CO₂ hydrogenation.^[19] Thanks to the previous reports, the most common understanding of the enhanced stability of intermetallics is from a static perspective, where the heteroatomic bonding in intermetallics tends to have a more negative formation enthalpy relative to the random alloys. However, catalysis is a dynamical process that involves multiple interactions between adsorbates and surface atoms of the catalyst. Therefore, exploring how the dynamic evolution of intermetallics influences the catalytic performance has great potential to offer a guideline for developing highly efficient catalysts.

Herein, we demonstrate that PdFe intermetallic nanocrystals enabled the maintenance of metallic Fe species via a reversible oxidation–reduction process in CO₂ methanation. The mass activity of *fcc*-PdFe nanocrystals reached 5.3 mmol g⁻¹ h⁻¹, under 1 bar (CO₂/H₂ = 1:4) at 180°C, being 6.6, 1.6, 3.3, and 5.3 times as high as that of *fcc*-PdFe nanocrystals, Ru/C, Ni/C, and Pd/C, respectively. Moreover, the activation energy for CO₂ methanation over PdFe intermetallic nanocrystals was 52.4 kJ mol⁻¹, which is significantly lower than that of the random alloy counterpart

[*] L. Luo,^[†] M. Wang,^[†] Y. Cui, Z. Chen, J. Wu, Y. Cao, J. Luo, Y. Dai, W.-X. Li, J. Bao, J. Zeng
Hefei National Laboratory for Physical Sciences at the Microscale, National Synchrotron Radiation Laboratory, CAS Key Laboratory of Strongly-Coupled Quantum Matter Physics, Key Laboratory of Surface and Interface Chemistry and Energy Catalysis of Anhui Higher Education Institutes, Department of Chemical Physics, University of Science and Technology of China
Hefei, Anhui 230026 (P. R. China)
E-mail: baoj@ustc.edu.cn
zengj@ustc.edu.cn

[†] These authors contributed equally to this work.

Supporting information and the ORCID identification number(s) for the author(s) of this article can be found under:
<https://doi.org/10.1002/anie.201916032>.

(81.1 kJ mol⁻¹). Even after 20 rounds of successive reaction (60 h in total), PdFe intermetallic nanocrystals still retained 98% of the original activity. Further mechanistic studies revealed that the reversible oxidation-reduction of surface Fe in PdFe intermetallic nanocrystals led to the maintenance of metallic Fe during the catalytic test. The metallic Fe in PdFe intermetallic nanocrystals enabled the direct conversion of CO₂ into CO* as the intermediate. As for PdFe random alloys, surface Fe was irreversibly oxidized, in which CO₂ was indirectly transformed into CO* via the formation of COOH*. The unique reaction path for PdFe intermetallic nanocrystals contributed to the lowered activation energy and thus the enhanced catalytic activity under atmospheric pressure.

Results and Discussion

To begin with, the nanocrystals with Pd cores and FeO_x shells (denoted as Pd@FeO_x nanocrystals) were prepared via seeded growth (Supporting Information, Figure S1). In a typical synthesis of PdFe intermetallic nanocrystals, the obtained Pd@FeO_x nanocrystals were loaded on activated carbon and annealed under a H₂/N₂ flow (H₂:N₂ = 1:9) with the rate of 50 sccm at 600 °C for 3 h. We proposed the following mechanism for the transformation from a core-shell structure to an alloy.^[20] In this reductive annealing condition, FeO_x shell was reduced to Fe metallic shell, accompanied with the formation of vacancies in the Fe lattice as a transient state (Supporting Information, Figure S2a). The vacancies facilitated the inter-diffusion between the Pd core and the Fe shell,

resulting in the formation of alloys. The obtained nanocrystals were uniformly dispersed on activated carbon, while the size varied from 6.8 to 9.3 nm with an average size of 8.0 nm (Supporting Information, Figure S2b). Figure 1a shows a representative high-angle annular dark-field scanning transmission electron microscopy (HAADF-STEM) image of an individual nanocrystal, as well as the corresponding fast Fourier transform (FFT) pattern recorded along the [100] zone axis. The lattice spacing was measured as 3.8 Å, which was assigned to the (001) facets exposed on the face-centered-tetragonal (*fcc*) PdFe nanocrystals. As shown in the magnified image, the nanocrystal took an intermetallic structure, which was revealed by the alternating bright (Pd) and dark (Fe) contrast on (001) facets (Figure 1b). The alternate distribution of Pd and Fe elements was further substantiated by the intensity profile along the line X–Y in the observed image (Figure 1c), as the signal intensity is approximately proportional to the square of atomic number.^[21] Moreover, the highly ordered nature of the nanocrystal was also verified by the HAADF-STEM image recorded along [110] zone axis (Supporting Information, Figure S3). For the analysis of the structures and chemical compositions of the nanostructure, the STEM and STEM-energy dispersive X-ray (EDX) elemental mapping images of PdFe intermetallic nanocrystals were shown in Figure 1d, indicating the homogenous distribution of both Pd and Fe. The cross-sectional compositional line-scanning profile of the nanocrystal in Figure 1d further proves the complete overlap of both elements without significant segregation of each component (Figure 1e). Based on the inductively coupled plasma-atomic emission spectroscopy (ICP-AES) measurements, the ratio of Pd to Fe in PdFe

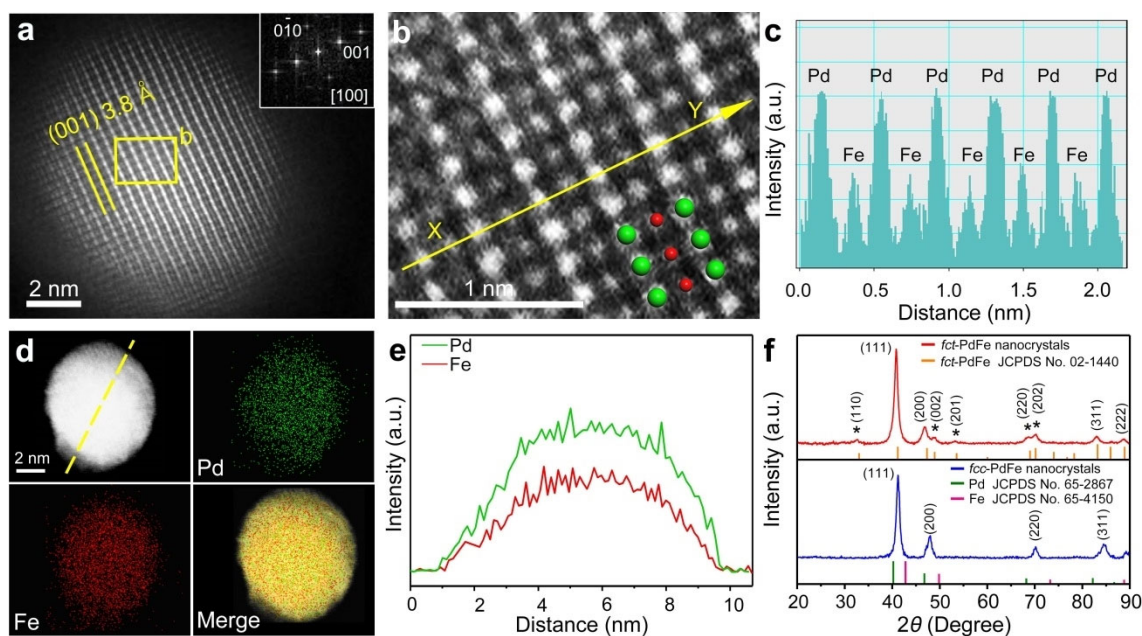


Figure 1. a) HAADF-STEM image of an individual *fcc*-PdFe nanocrystal. Inset: corresponding FFT pattern with the electron beam directed along the [100] axis and an atomic model of a unit cell. b) Magnified HAADF-STEM images from the yellow box in (a). Pd green, Fe red spheres. c) Intensity profile along the line X–Y in the magnified HAADF-STEM image in (b). d) STEM image and STEM-EDX elemental mapping images of an individual *fcc*-PdFe nanocrystal. e) Compositional line profile of Pd and Fe from the *fcc*-PdFe nanocrystal recorded along the line shown in (d). f) XRD patterns of *fcc*-PdFe nanocrystals and *fcc*-PdFe nanocrystals.



intermetallic nanocrystals was determined to be 49:51, while the mass loading of PdFe intermetallic nanocrystals was 5.2%. The XRD pattern of PdFe intermetallic nanocrystals shows the characteristic peaks, which well corresponded to PdFe intermetallics in the *fcc* structure (JCPDS No. 02-1440) as shown in Figure 1 f. The atomic model of PdFe intermetallic nanocrystals, where Pd and Fe are intermetallically stacked, is shown in the Supporting Information, Figure S4. Specifically, when Fe was equiatomicly alloyed with Pd to form an intermetallic compound, the phase took an $L1_0$ structure which was an ordered *fcc* structure with tetragonal distortion (Supporting Information, Table S1). For simplification, the obtained nanocrystals were denoted as *fcc*-PdFe nanocrystals. Based on Rietveld refinement, the size of *fcc*-PdFe nanocrystals was calculated as 9.3 nm, slightly larger than the particle sizes (8.0 nm) determined by TEM. An average size of 9.3 nm (XRD) and 8.0 nm (TEM) are close enough, considering the uncertainty of the measurements and the nanoparticle size distribution. Furthermore, the ratio of surface-active atoms to total atoms in *fcc*-PdFe nanocrystals was determined as 12.9% by CO pulse chemisorptions (Supporting Information, Figure S5).

PdFe random alloys were also prepared based on the method similar to that for *fcc*-PdFe nanocrystals, except for the annealing temperature lowered to 400 °C. The obtained alloys were well dispersed on activated carbon, while the size ranged from 6.3 to 8.8 nm with an average size of 7.9 nm (Supporting Information, Figure S2c). As shown in the HAADF-STEM images, alternating bright and dark contrasts were not observed, indicating the disordered atomic arrangement in the obtained nanocrystals (Supporting Information, Figure S6a,b). The lattice spacing of 2.2 Å corresponded to the (111) facets of the face-centered-cubic (*fcc*) PdFe nanocrystals. As shown in the Supporting Information, Figure S7, Fe atoms randomly substitute for half of the Pd atoms in *fcc*-Pd nanocrystals to form a common lattice in $A1$ phase with the space group of $Fm\bar{3}m$. The irregular intensity profiles in different directions further demonstrated the random distribution of Pd and Fe elements (Supporting Information, Figure S6b,c). Besides, both Pd and Fe were homogeneously distributed as revealed by the STEM image, STEM-EDX elemental mapping images, and the corresponding compositional line-scanning (Figure S6e,f). Moreover, the random alloy structure in *fcc* phase was further verified by the XRD pattern (Figure 1 f), as the characteristic peaks of the obtained nanocrystals all lie amid the peak positions of *fcc* Pd (JCPDS No. 65-2867) and *fcc* Fe (JCPDS No. 65-4150). According to Rietveld refinement, the size of *fcc*-PdFe nanocrystals was calculated as 8.8 nm. Based on the quantitative phase analysis, the content of Pd in PdFe random alloys was estimated as ca. 50% (Supporting Information, Figure S8). The ratio of Pd to Fe in PdFe random alloys was further determined to be 50:50 by ICP-AES, consistent with the quantitative phase analysis, while the mass loading of PdFe nanocrystals was 4.8 wt%. For simplification, the random alloys were denoted as *fcc*-PdFe nanocrystals. For comparison, commercial Ru/C with an average size of 2.4 nm and Pd/C with an average size of 4.0 nm were obtained at a mass loading of 5.0 wt% (Supporting Information, Fig-

ure S9a,b). We also prepared Ni/C with an average size of 8.0 nm and a mass loading of 5.0 wt% (Supporting Information, Figure S10). Furthermore, the ratios of surface active atoms to total metal atoms in *fcc*-PdFe nanocrystals, Ru/C, Ni/C, and Pd/C were determined as 13.0%, 35.5%, 15.3%, and 29.1%, respectively, by CO pulse chemisorptions and H₂ pulse chemisorptions (Supporting Information, Figure S5).

The *fcc*-PdFe nanocrystals were applied in CO₂ hydrogenation, in comparison with *fcc*-PdFe nanocrystals and commercial Ru/C, Ni/C, and Pd/C. For a catalytic test, the weights of *fcc*-PdFe nanocrystals, *fcc*-PdFe nanocrystals, Ru/C, Ni/C, and Pd/C were controlled at 0.85, 0.85, 7.8, 10.5, and 10.0 mg, respectively, so as to keep the same amount (1.37 μmol) of surface metal atoms in each catalyst. The reaction was conducted in the slurry reactor under 1 bar of CO₂/H₂ mixed gas (CO₂/H₂ = 1:4) at 180 °C. GC calibration was carried out before the tests with the use of standard gases with known concentrations (Supporting Information, Figure S11). When the reaction proceeded over blank reactor or activated carbon, the products after 3 h were below the detection limit, thereby demonstrating the inertness of the reactor and excluding the influence of the supports (Supporting Information, Figures S12, S13). Methane was produced over these Pd-based nanocrystals and commercial catalysts without the formation of other products (Supporting Information, Figures S14–S18). After 3 h, the yields of methane for *fcc*-PdFe nanocrystals, *fcc*-PdFe nanocrystals, Ru/C, Ni/C, and Pd/C were 0.26, 0.04, 0.08, 0.05, and 0.03 mmol, respectively (Figure 2 a). Moreover, the corresponding turnover numbers (TON) were 189.8, 29.2, 58.4, 36.5, and 21.9, respectively. To compare the catalytic activity more accurately, we calculated the mass activity and turnover frequency (TOF) numbers of these catalysts based on the reaction profile at the initial stage and the amounts of surface-active atoms. The mass activity of *fcc*-PdFe nanocrystals reached 5.3 mmol g⁻¹ h⁻¹ at 180 °C, being 6.6, 1.6, 3.3, and 5.3 times as high as that of *fcc*-PdFe nanocrystals, Ru/C, Ni/C, and Pd/C, respectively (Supporting Information, Figure S19). The TOF number of *fcc*-PdFe nanocrystals reached 86 h⁻¹ at 180 °C, being 7.4, 4.4, 6.9, and 11.0 times as high as that of *fcc*-PdFe nanocrystals, Ru/C, Ni/C, and Pd/C, respectively (Supporting Information, Figure S19). These results demonstrated that *fcc*-PdFe nanocrystals served as a promising catalyst towards CO₂ methanation, especially at low temperatures (Supporting Information, Tables S2, S3).

To further explore the catalytic properties of PdFe nanocrystals, we conducted a series of catalytic tests under 1 bar of CO₂/H₂ mixed gas (CO₂/H₂ = 1:4) at different temperatures. As shown in Figure 2 b, *fcc*-PdFe nanocrystals exhibited much higher catalytic activity than *fcc*-PdFe nanocrystals. Moreover, *fcc*-PdFe nanocrystals were active even at 100 °C, whereas for *fcc*-PdFe nanocrystals, products were only detected at above 140 °C, respectively. Arrhenius plots were obtained based on the linear fitting of ln(TOF) versus 1000/T. The activation energies for CO₂ methanation over *fcc*-PdFe nanocrystals and *fcc*-PdFe nanocrystals were determined as 52.4 and 81.1 kJ mol⁻¹, respectively (Figure 2 c).

We further explored whether CH₄ was sourced from CO₂ or activated carbon. We conducted catalytic tests under 1 bar



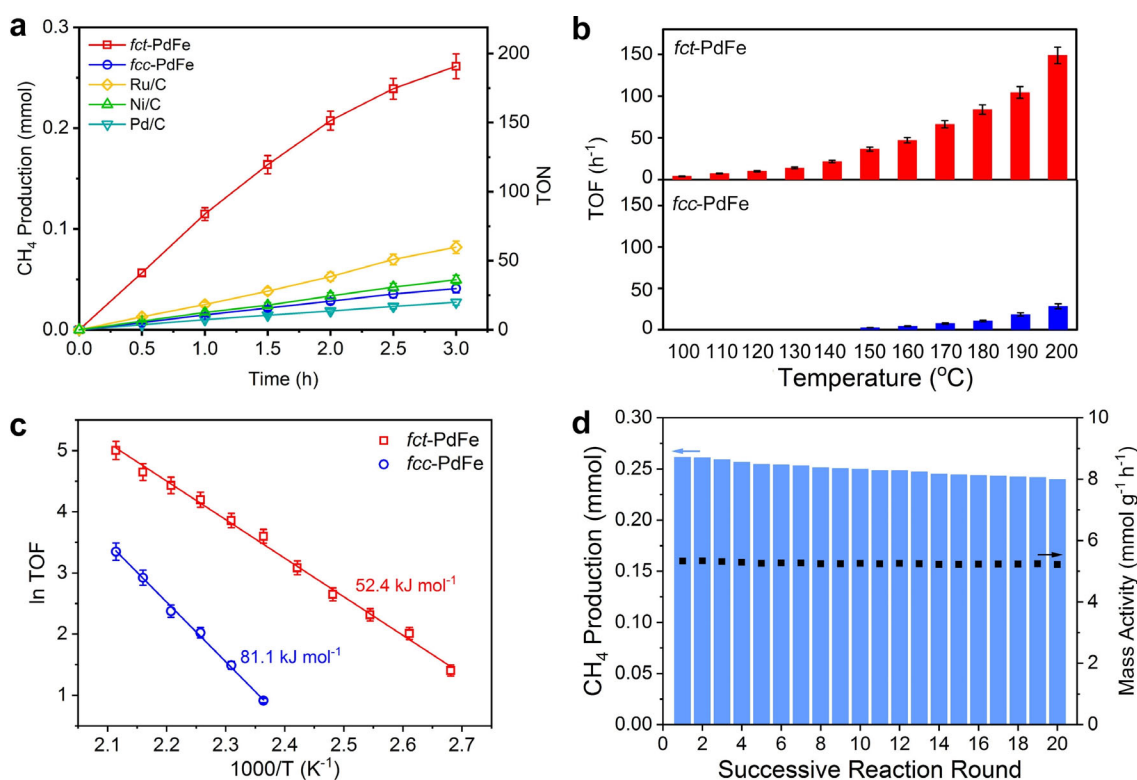


Figure 2. a) Time courses and TON numbers for *fct*-PdFe nanocrystals, *fcc*-PdFe nanocrystals, Ru/C, Ni/C, and Pd/C under 1 bar of CO₂/H₂ mixed gas (CO₂:H₂ = 1:4) at 180 °C. b) Comparison in TOF numbers of *fct*-PdFe nanocrystals and *fcc*-PdFe nanocrystals. The reaction tests were pressurized with CO₂/H₂ mixed gas (CO₂:H₂ = 1:4, 1 bar). c) Arrhenius plots of *fct*-PdFe nanocrystals and *fcc*-PdFe nanocrystals. d) Product yields of *fct*-PdFe nanocrystals over the course of 20 rounds of successive reaction. Error bars represent standard deviation from three independent measurements.

of N₂/H₂ mixed gas (N₂/H₂ = 1:4) at 180 °C for 3 h. As shown in the Supporting Information, Figure S20, both the gaseous and liquid products were below detection limit, indicating the inertness of the activated carbon. Furthermore, isotropic labeled experiment using labeled ¹³CO₂ as the reactant over *fct*-PdFe nanocrystals was performed to demonstrate the origin of the carbon source. The mass spectrum of gaseous products with the use of ¹²CO₂ or ¹³CO₂ as a reactant is shown in the Supporting Information, Figure S21. When ¹²CO₂ was applied as a reactant, the intensity of the peak at *m/z* = 16 was stronger than that for ¹²CH₄ (NIST MS 61313), owing to the baseline signal of O⁺ from the ionization of ¹²CO₂. In this case, the peak at *m/z* = 16 could not be applied to identify the produced ¹²CH₄, so that we used the peak at *m/z* = 12 to identify ¹²CH₄. When the reactant was replaced by ¹³CO₂, the peak at *m/z* = 12 was negligible, indicating the activated carbon containing ¹²C did not participated in the reaction. Moreover, a new peak at *m/z* = 17 appeared, indicating the generation of ¹³CH₄. Moreover, the carbon balance was calculated as 98.6 % (Supporting Information, Table S4). Therefore, methane was formed only by CO₂ hydrogenation.

To investigate stability of the catalysts, we conducted HAADF-STEM characterizations of PdFe nanocrystals after CO₂ hydrogenation at 180 °C for 3 h. As for the used *fct*-PdFe nanocrystals (used refers to the catalyst after one cycle), the alternative bright and dark contrasts in the HAADF-STEM image were preserved (Supporting Information, Figure S22a),

indicating the retained intermetallic structure. The cross-sectional compositional line-scanning profile of an individual *fct*-PdFe nanocrystal demonstrated the homogeneous distribution of Pd and Fe (Supporting Information, Figure S22b). As such, *fct*-PdFe nanocrystals were determined to be highly stable during catalytic tests. With regard to the used *fcc*-PdFe nanocrystals, the surface became rich in Fe species owing to the oxidation of surface Fe species (Supporting Information, Figure S22c,d). Furthermore, we further performed successive rounds of reaction over *fct*-PdFe nanocrystals. After twenty rounds, the original mass activity of *fct*-PdFe nanocrystals was preserved (Figure 2d). Further characterizations of *fct*-PdFe nanocrystals showed that they were still homogeneously dispersed on the support, while the intermetallic structure was well-retained (Supporting Information, Figure S23). Therefore, *fct*-PdFe nanocrystals exhibited remarkable stability during CO₂ hydrogenation.

To investigate the interaction between the PdFe nanocrystals and reactants, we conducted quasi situ X-ray photoelectron spectroscopy (XPS) measurements. Figure 3a shows the Fe 2p spectra of *fct*-PdFe nanocrystals, where Fe species were determined at the metallic state (Fe⁰) without any treatment.^[22] After the treatment of *fct*-PdFe nanocrystals with CO₂ at 180 °C for 30 min, the ratio of the oxidized Fe (Fe^{x+}) to Fe⁰ significantly increased, indicating the partial oxidation of surface Fe species (Figure 3a). The surface Fe^{x+} on *fct*-PdFe nanocrystals could be facily reduced back to the



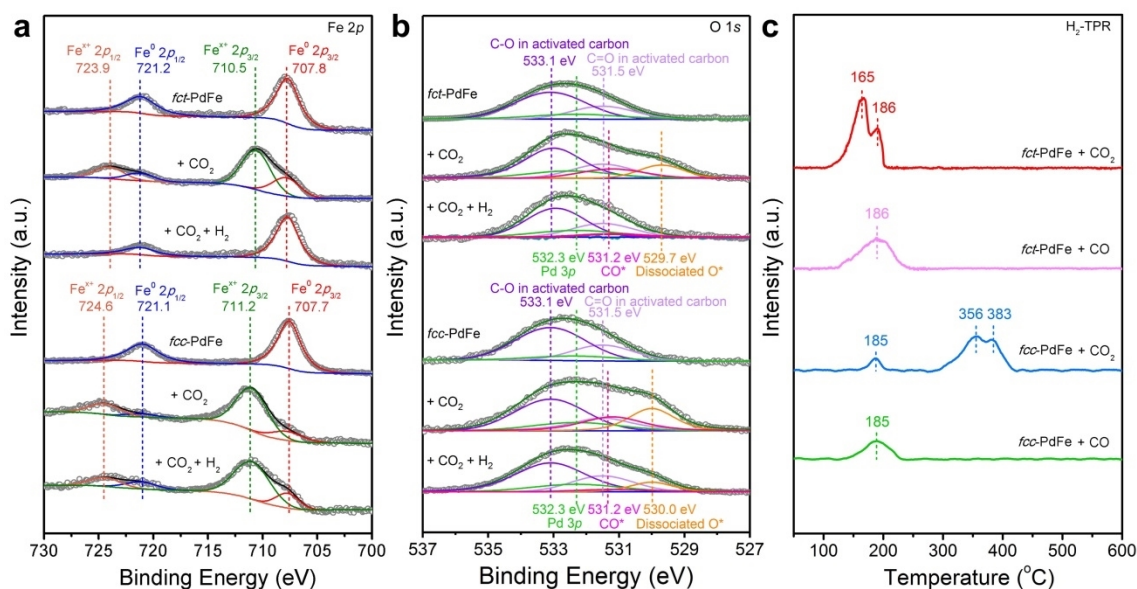


Figure 3. a) Quasi situ XPS spectra of Fe 2p for *fct*-PdFe and *fcc*-PdFe nanocrystals before and after the treatment with CO₂ as well as CO₂ and H₂ in sequence at 180 °C for 30 min. b) Quasi situ XPS spectra of O 1s for *fct*-PdFe and *fcc*-PdFe nanocrystals before and after the treatment with CO₂ as well as CO₂ and H₂ in sequence at 180 °C for 30 min. c) H₂-TPR profiles of *fct*-PdFe nanocrystals and *fcc*-PdFe nanocrystals after the treatment with CO₂ and CO at 180 °C for 30 min.

Fe⁰ by H₂ treatment at 180 °C for 30 min (Figure 3a). As for *fcc*-PdFe nanocrystals, the surface Fe⁰ was also able to be oxidized into Fe²⁺ after the exposure to CO₂ at 180 °C for 30 min (Figure 3b). Different from the case of *fct*-PdFe nanocrystals, the surface Fe²⁺ on *fcc*-PdFe nanocrystals resisted the reduction back into Fe⁰ by H₂ treatment at 180 °C for 30 min (Figure 3b). As such, the oxidation–reduction of surface Fe on *fct*-PdFe nanocrystals was reversible during CO₂ hydrogenation, whereas that on *fcc*-PdFe nanocrystals was irreversible.

We also compared Pd 3d XPS spectra of *fct*-PdFe and *fcc*-PdFe nanocrystals before/after different gas treatment. Specifically, the Pd species in *fct*-PdFe nanocrystals were determined in metallic state before any treatment (Supporting Information, Figure S23). After the treatment with H₂, Pd 3d_{3/2} and 3d_{5/2} peaks were shifted to higher binding energies (Supporting Information, Figure S23). The positive shifts were induced by the adsorption of CO₂ or the dissociated O* species. After further treatment with H₂, the peaks were shifted back to the binding energies of those before any treatment, indicating the reduction of oxidized Pd species into metallic states. As for *fcc*-PdFe nanocrystals, the Pd 3d XPS spectra after different treatment behaved similarly to those of *fct*-PdFe nanocrystals in terms of peak positions (Supporting Information, Figure S24). Therefore, both *fct*-PdFe and *fcc*-PdFe nanocrystals enabled the reversible oxidation–reduction of Pd in CO₂ methanation.

We further recorded O 1s XPS spectra of *fct*-PdFe nanocrystals and *fcc*-PdFe nanocrystals before/after different gas treatment. As the nanocrystals were supported on activated carbon to prevent sintering during the annealing process, the peaks of C–O and C=O species in the support and Pd 3p were observed in O 1s XPS spectra before the treatment (Figure 3b).^[23–26] As shown in the O 1s XPS spectra of *fct*-PdFe

nanocrystals after the treatment with CO₂, the peak at 531.2 eV and 529.7 eV appeared, corresponding to the CO* and dissociated O* species, respectively (Figure 3b).^[27–29] These two peaks were also observed for *fcc*-PdFe nanocrystals after the treatment with CO₂. After the reduction in H₂, the peak intensity for CO* species was weakened for *fct*-PdFe nanocrystals, indicating the consumption of CO. Meanwhile, the peak for dissociated O* species disappeared, demonstrating the reversible oxidation–reduction process for Fe species (Figure 3b). In comparison, the peak at 530.0 eV for dissociated O* species still remained for *fcc*-PdFe nanocrystals, which was ascribed to the irreversible oxidation of Fe species.

To investigate whether the oxidized Fe species could be facilely reduced by H₂, we conducted the measurements of H₂ temperature-programmed reduction (H₂-TPR). As shown in Figure 3c, two peaks were observed in the H₂-TPR profile of *fct*-PdFe nanocrystals after the treatment with CO₂. The peak at 165 °C was assigned to the reduction of surface FeO_x species. In this case, the O* species could be facilely consumed by H₂, and thus were weakly bonded with Fe. The other peak at 186 °C derived from the hydrogenation of adsorbed CO* species, which was confirmed by the H₂-TPR profile of *fct*-PdFe nanocrystals after the treatment with CO. When *fcc*-PdFe nanocrystals were treated with CO₂ prior to H₂-TPR, three peaks were observed. Specifically, the peak at 185 °C corresponded to the hydrogenation of CO*, as evidenced by the H₂-TPR profile of *fcc*-PdFe nanocrystals after the exposure to CO (see details in the Supporting Information, Experimental Section). The peaks at 356 and 383 °C were assigned to the reduction of different Fe oxides. As such, the reduction of oxidized Fe species on *fcc*-PdFe nanocrystals requires much higher temperature than that on *fct*-PdFe nanocrystals.

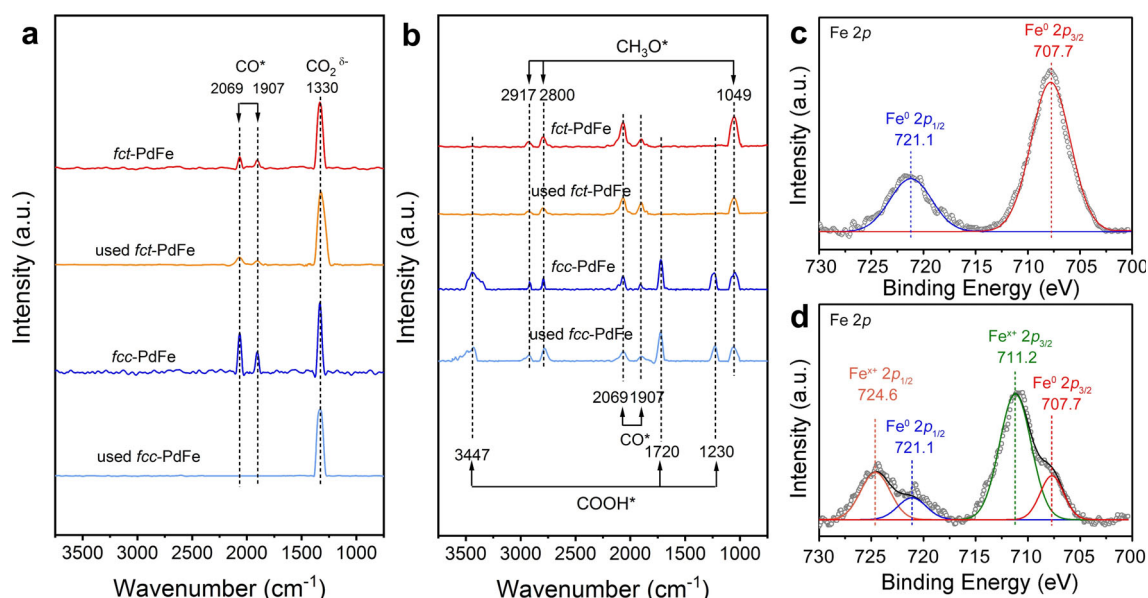


Figure 4. a), b) In situ DRIFTS spectra of *fct*-PdFe nanocrystals, used *fct*-PdFe nanocrystals, *fcc*-PdFe nanocrystals, and used *fcc*-PdFe nanocrystals after the treatment with a) CO₂ at 180 °C for 30 min and b) CO₂/H₂ mixed gas (CO₂:H₂ = 1:4) at 180 °C for 30 min. c), d) Quasi situ XPS spectra of Fe 2p for *fct*-PdFe and *fcc*-PdFe nanocrystals after the treatment with CO₂/H₂ mixed gas (CO₂:H₂ = 1:4) at 180 °C for 30 min.

To gain deep insight into the reaction paths, we further conducted in situ diffuse reflectance infrared Fourier transform (DRIFTS) measurements. The in situ DRIFTS spectra of *fct*-PdFe nanocrystals and *fcc*-PdFe nanocrystals after the treatment with CO₂ at 180 °C for 30 min exhibited two sets of characteristic peaks (Figure 4a; Supporting Information, Figure S25, Table S5). One set of peaks located at 2069 and 1907 cm⁻¹ corresponded to CO* adsorbed in linear and bridged forms, respectively.^[30–33] The other set of peak at 1330 cm⁻¹ was assigned to the stretching vibration of CO₂^{δ-} species.^[34–37] With regard to *fct*-PdFe and *fcc*-PdFe nanocrystals, both CO* and CO₂^{δ-} species were detected (Figures 3b and 4a). As such, the PdFe alloys enabled the direct dissociation of CO₂ into CO*. Considering the surface reconstruction of *fcc*-PdFe nanocrystals during catalytic testing, we further investigated the adsorption properties of CO₂ on the used *fct*-PdFe and the used *fcc*-PdFe nanocrystals after one cycle of CO₂ hydrogenation at 180 °C for 3 h. The peaks for the used *fct*-PdFe nanocrystals were consistent with those of the fresh one. In contrast, CO* species was not detected by in situ DRIFTS measurements after the exposure of the used *fcc*-PdFe nanocrystals to CO₂ (Figure 4a). Therefore, the direct dissociation of CO₂ into CO* only occurred on Fe⁰ rather than Fe^{x+}.

We further treated *fct*-PdFe nanocrystals, *fcc*-PdFe nanocrystals, and used *fcc*-PdFe nanocrystals with CO₂/H₂ mixed gas (CO₂/H₂ = 1:4) for 30 min before in situ DRIFTS measurements. Figure 4b showed three sets of characteristic peaks. Besides the peaks at 2069 and 1907 cm⁻¹ for CO*, the set of peaks at 2917, 2800, and 1049 cm⁻¹ were assigned to the stretching vibration of C–H, the bending vibration of C–H, and the stretching vibration of C–O in CH₃O* species, respectively.^[38–41] The peaks at 3447, 1720, and 1230 cm⁻¹ arose from the stretching vibrations of O–H, C=O, and C–O in COOH* species, respectively.^[42–45] As for *fct*-PdFe

nanocrystals, CO* and CH₃O* species were detected. In comparison, COOH*, CO*, and CH₃O* species were all observed for the *fcc*-PdFe nanocrystals and used *fcc*-PdFe nanocrystals. The similarity of in situ spectra of *fcc*-PdFe and used *fcc*-PdFe nanocrystals was attributed to the rapid reconstruction of *fcc*-PdFe nanocrystals. To support this point, we implemented in situ DRIFTS measurements after exposing *fcc*-PdFe nanocrystals to CO₂/H₂ mixed gas for different periods of time. After the treatment for 5 min, the peaks for CO* and CH₃O* species were observed (Supporting Information, Figure S25). With the treatment time prolonged to 15 and 30 min, new peaks for COOH* emerged (Supporting Information, Figure S25). As such, we proposed the reaction paths for PdFe nanocrystals as shown in the Supporting Information, Scheme S1. For *fct*-PdFe nanocrystals, methane was produced via the subsequent transformation of CO₂ into CO* and CH₃O* species. In comparison, *fcc*-PdFe nanocrystals were quickly oxidized within 15 min, over which CO₂ was subsequently converted into COOH*, CO*, and CH₃O* to form methane. The direct conversion of CO₂ into CO* without the formation of COOH* for *fct*-PdFe nanocrystals derived from the maintenance of Fe⁰ during the catalytic test. The unique reaction path for *fct*-PdFe nanocrystals contributed to the lowered activation energy and thus the enhanced catalytic activity under atmospheric pressure. Furthermore, after the treatment of *fct*-PdFe and *fcc*-PdFe nanocrystals with CO₂/H₂ mixed gas (CO₂/H₂ = 1:4), the XPS spectra resembled those after the treatment with CO₂ and H₂ in sequence (Figure 4c,d). These results indicate the reversible oxidation-reduction of surface Fe on *fct*-PdFe nanocrystals and irreversible oxidation on *fcc*-PdFe nanocrystals during CO₂ hydrogenation.

We further conducted density functional theory (DFT) calculations to investigate the origin of the difference between *fct*-PdFe and *fcc*-PdFe nanocrystals. To simulate



the random alloys, we regarded *fcc*-PdFe nanocrystals as a solid solution composed of phases with different Pd/Fe ratios including *fcc*-Pd, *fcc*-Pd₃Fe₁, *fcc*-PdFe, *fcc*-Pd₁Fe₃, and *fcc*-Fe (Supporting Information, Figure S26). To minimize the total surface energy, these nanocrystals are expected to take a truncated octahedral morphology enclosed by a mixture of (111) and (100) facets. Notably, surface percentage of atoms on (111) facets can reach 70% for an 8 nm particle based on theoretical model. In this regard, we firstly paid attention to the (111) facet which is exposed on most of the surfaces of *fcc*-PdFe and *fcc*-PdFe nanocrystals.^[46–48]

The transformation of CO₂ into COOH* is an exothermic process for the (111) surface of all crystal phases (Supporting Information, Figures S27–S29). The dissociation of CO₂ into CO* and O* is energetically unfavorable on *fcc*-Pd(111) and *fcc*-Pd₃Fe₁(111) surfaces. This process is exothermic on *fcc*-PdFe(111), *fcc*-Pd₁Fe₃(111), and *fcc*-Fe(111) surfaces. On these surfaces, the enthalpy variation of CO₂ dissociation was more negative than that of the formation of COOH*. As such, CO₂ directly dissociates into CO* and O* on surfaces rich in Fe component and *fcc*-PdFe(111) surface, whereas CO₂ is hydrogenated into COOH* on surfaces rich in Pd component. We further calculated the energy on the reduction of O*. As shown in the Supporting Information, Figure S28, the enthalpy variation decreases with the content of Pd. Notably, the reduction process is thermodynamically unfavorable on *fcc*-Fe(111) and *fcc*-Pd₁Fe₃(111) surfaces, whereas that is exothermic on *fcc*-PdFe(111), *fcc*-Pd₃Fe₁(111), and Pd(111) surfaces. In this case, once the surfaces were oxidized, *fcc*-PdFe(111) surfaces could be facily reduced. As for surfaces on *fcc* nanocrystals, those rich in Fe component were hard to be reduced, whereas those rich in Pd component allowed for the recovery into the metallic states.

We also investigated the influence of {100} facets which are less stable than {111} facets but more stable than {110} facets.^[47] For *fcc*-Fe(100) and *fcc*-Pd₁Fe₃(100) surfaces, H-assisted dissociation is exothermic (Supporting Information, Figure S30). Although direct dissociation of CO₂ is also exothermic, the reduction of O* is thermodynamically unfavorable. As for *fcc*-PdFe(010) surface, both H-assisted dissociation and direct dissociation of CO₂ are energetically unfavorable. As such, *fcc*-PdFe(010) surface is inert for CO₂ activation. In other words, the reaction mainly occurs on *fcc*-PdFe(111) surface which adopts the direct conversion of CO₂. With regard to *fcc*-Pd₃Fe₁(100) and *fcc*-Pd(100) surfaces, H-assisted dissociation of CO₂ is exothermic, whereas direct dissociation is endothermic. Collectively, except for inert *fcc*-PdFe(010) surface, all the other (100) surfaces adopt the transformation of CO₂ into COOH*, consistent with the reaction path on {111} facets.

Conclusion

We have reported an efficient catalyst of PdFe intermetallic nanocrystals towards CO₂ methanation. During CO₂ hydrogenation, *fcc*-PdFe nanocrystals significantly enhanced the catalytic activity and decreased the activation energy relative to *fcc*-PdFe nanocrystals. The high catalytic activity of

fcc-PdFe nanocrystals was associated with their unique reaction path. Mechanistic studies revealed that *fcc*-PdFe nanocrystals ensuring renewable metallic surfaces followed the direct dissociation of CO₂ into CO* and O*. As for *fcc*-PdFe nanocrystals, both direct dissociation into CO* and H-assisted dissociation into COOH* existed during the initial stage of reaction. Upon the irreversible oxidation of surface metallic Fe species on *fcc*-PdFe nanocrystals, CO₂ was only hydrogenated into COOH*, while the direct dissociation route was suppressed. Our understanding on how the electronic structures of intermetallics influence the catalytic performance has great potential to offer a guideline for developing highly efficient catalysts.

Acknowledgements

This work was supported by National Science Fund for Distinguished Young Scholars (21925204), NSFC (U19A2015, U1732272, and 21673214), National Key Research and Development Program of China (2019YFA0405600), Key Research Program of Frontier Sciences of the CAS (QYZDB-SSW-SLH017), Major Program of Development Foundation of Hefei Center for Physical Science and Technology (2017FXZY002), Fundamental Research Funds for the Central Universities, and USTC Research Funds of the Double First-Class Initiative (YD2340002002).

Conflict of interest

The authors declare no conflict of interest.

Keywords: CO₂ hydrogenation · intermetallic nanocrystals · iron · palladium

- [1] R. B. Jackson, J. G. Canadell, C. L. Quéré, R. M. Andrew, J. I. Korsbakken, G. P. Peters, N. Nakicenovic, *Nat. Clim. Change* **2016**, *6*, 7–10.
- [2] R. C. Armstrong, C. Wolfram, K. P. de Jong, R. Gross, N. S. Lewis, B. Boardman, A. J. Ragauskas, K. Ehrhardt-Martinez, G. Crabtree, M. V. Ramana, *Nat. Energy* **2016**, *1*, 15020.
- [3] C. Vogt, E. Groeneveld, G. Kamsma, M. Nachtegaal, L. Lu, C. J. Kiely, P. H. Berben, F. Meirer, B. M. Weckhuysen, *Nat. Catal.* **2018**, *1*, 127–134.
- [4] M. Ghoussoub, M. Xia, P. N. Duchesne, D. Segal, G. Ozin, *Energy Environ. Sci.* **2019**, *12*, 1122–1142.
- [5] C. Yan, H. Li, Y. Ye, H. Wu, F. Cai, R. Si, J. Xiao, S. Miao, S. Xie, F. Yang, Y. Li, G. Wang, X. Bao, *Energy Environ. Sci.* **2018**, *11*, 1204–1210.
- [6] T. Abe, M. Tanizawa, K. A. Watanabe, *Energy Environ. Sci.* **2009**, *2*, 315–321.
- [7] C. Vogt, M. Monai, G. J. Kramer, B. M. Weckhuysen, *Nat. Catal.* **2019**, *2*, 188–197.
- [8] P. Sabatier, J.-B. Senderens, *C. R. Hebd. Seances Acad. Sci.* **1903**, *134*, 689–691.
- [9] C. Li, S. Zhang, B. Zhang, D. Su, S. He, Y. Zhao, J. Liu, F. Wang, M. Wei, D. G. Evans, X. Duan, *J. Mater. Chem. A* **2013**, *1*, 2461–2467.



- [10] F. Wang, S. He, H. Chen, B. Wang, L. Zheng, M. Wei, D. G. Evans, X. Duan, *J. Am. Chem. Soc.* **2016**, *138*, 6298–6305.
- [11] M. D. Marcinkowski, M. T. Darby, J. Liu, M. J. Wimple, F. R. Lucci, S. Lee, A. Michaelides, M. Flytzani-Stephanopoulos, M. Stamatakis, E. C. H. Sykes, *Nat. Chem.* **2018**, *10*, 325–332.
- [12] A. Holewinski, J. C. Idrobo, S. Linic, *Nat. Chem.* **2014**, *6*, 828–834.
- [13] F. Tao, *Chem. Soc. Rev.* **2012**, *41*, 7977–7979.
- [14] Q. Jia, J. Li, K. Caldwell, D. E. Ramaker, J. M. Ziegelbauer, R. S. Kukreja, A. Kongkanand, S. Mukerjee, *ACS Catal.* **2016**, *6*, 928–938.
- [15] W. Luo, M. Sankar, A. M. Beale, Q. He, C. J. Kiely, P. C. A. Bruijninx, B. M. Weckhuysen, *Nat. Commun.* **2015**, *6*, 6540.
- [16] F. Studt, I. Sharafutdinov, F. Abild-Pedersen, C. F. Elkjær, J. S. Hummelshøj, S. Dahl, I. Chorkendorff, J. K. Nørskov, *Nat. Chem.* **2014**, *6*, 320–324.
- [17] D. Wang, H. L. Xin, R. Hovden, H. Wang, Y. Yu, D. A. Muller, F. J. DiSalvo, H. D. Abruña, *Nat. Mater.* **2013**, *12*, 81–87.
- [18] A. García-Trenco, A. Regoutz, E. R. White, D. J. Payne, M. S. P. Shaffer, C. K. Williams, *Appl. Catal. B* **2018**, *220*, 9–18.
- [19] I. Sharafutdinov, C. F. Elkjær, H. W. P. de Carvalho, D. Gardini, G. L. Chiarello, C. D. Damsgaard, J. B. Wagner, J.-D. Grunwaldt, S. Dahl, I. Chorkendorff, *J. Catal.* **2014**, *320*, 77–88.
- [20] A. Kirkeminde, R. Shenqiang, *Nano Lett.* **2014**, *14*, 4493–4498.
- [21] S. J. Pennycook, D. E. Jesson, *Ultramicroscopy* **1991**, *37*, 14–38.
- [22] Ö. Metin, A. Mendoza-Garcia, D. Dalmizrak, M. S. Gültekin, S. Sun, *Catal. Sci. Technol.* **2016**, *6*, 6137–6143.
- [23] D. Momodu, A. Bello, K. Oyedotun, F. Ochai-Ejeh, J. Dangbegnon, M. Madito, N. Manyala, *RSC Adv.* **2017**, *7*, 37286–37295.
- [24] K. B. Hatzell, M. C. Hatzell, K. M. Cook, M. Boota, G. M. Housel, A. McBride, E. C. Kumbur, Y. Gogotsi, *Environ. Sci. Technol.* **2015**, *49*, 3040–3047.
- [25] F. U. Hillebrecht, J. C. Fuggle, P. A. Bennett, Z. Zolnierok, *Phys. Rev. B* **1983**, *27*, 2179–2193.
- [26] H. Gabasch, W. Unterberger, K. Hayek, B. Klötzer, E. Kleimeinov, D. Teschner, S. Zafeirotos, M. Hävecker, A. Knop-Gericke, R. Schlögl, J. Han, F. H. Ribeiro, B. Aszalos-Kiss, T. Curtin, D. Zemlyanov, *Surf. Sci.* **2006**, *600*, 2980–2989.
- [27] Y.-P. Sun, X.-Q. Li, W.-X. Zhang, H. P. Wang, *Colloids Surf. A* **2007**, *308*, 60–66.
- [28] F. Li, J. Li, L. Gao, Y. Hu, X. Long, S. Wei, C. Wang, J. Jin, J. Ma, *J. Mater. Chem. A* **2018**, *6*, 23478–23485.
- [29] S. Duan, R. Wang, J. Liu, *Nanotechnology* **2018**, *29*, 204002.
- [30] X. Wang, H. Shi, J. H. Kwak, J. Szanyi, *ACS Catal.* **2015**, *5*, 6337–6349.
- [31] S. E. Collins, J. J. Delgado, C. Mira, J. J. Calvino, S. Bernal, D. L. Chiavassa, M. A. Baltanás, A. L. Bonivardi, *J. Catal.* **2012**, *292*, 90–98.
- [32] A. Sápi, G. Halasi, J. Kiss, D. G. Dobó, K. L. Juhász, V. J. Kolcsár, Z. Ferencz, G. Vári, V. Matolin, A. Erdóhelyi, Á. Kukovecz, Z. Kónya, *J. Phys. Chem. C* **2018**, *122*, 5553–5565.
- [33] M. Bäumer, J. Libuda, K. M. Neyman, N. Rösch, G. Rupprechter, H.-J. Freund, *Phys. Chem. Chem. Phys.* **2007**, *9*, 3541–3558.
- [34] J. Graciani, K. Mudiyansele, F. Xu, A. E. Baber, J. Evans, S. D. Senanayake, D. J. Stacchiola, P. Liu, J. Hrbek, J. F. Sanz, J. A. Rodriguez, *Science* **2014**, *345*, 546–550.
- [35] M. U. Khan, L. Wang, Z. Liu, Z. Gao, S. Wang, H. Li, W. Zhang, M. Wang, Z. Wang, C. Ma, J. Zeng, *Angew. Chem. Int. Ed.* **2016**, *55*, 9548–9552; *Angew. Chem.* **2016**, *128*, 9700–9704.
- [36] L. Wang, W. Zhang, X. Zheng, Y. Chen, W. Wu, J. Qiu, X. Zhao, X. Zhao, Y. Dai, J. Zeng, *Nat. Energy* **2017**, *2*, 869–876.
- [37] Y. Peng, L. Wang, Q. Luo, Y. Cao, Y. Dai, Z. Li, H. Li, X. Zheng, W. Yan, J. Yang, J. Zeng, *Chem* **2018**, *4*, 613–625.
- [38] Y. Wang, S. Kattel, W. Gao, K. Li, P. Liu, J. G. Chen, H. Wang, *Nat. Commun.* **2019**, *10*, 1166.
- [39] S. Kattel, B. Yan, Y. Yang, J. G. Chen, P. Liu, *J. Am. Chem. Soc.* **2016**, *138*, 12440–12450.
- [40] J. Wang, G. Li, Z. Li, C. Tang, Z. Feng, H. An, H. Liu, T. Liu, C. Li, *Sci. Adv.* **2017**, *3*, e1701290.
- [41] C. Wang, P. Chen, Y. Li, G. Zhao, Y. Liu, Y. Lu, *J. Catal.* **2016**, *344*, 173–183.
- [42] Y. Chen, H. Li, W. Zhao, W. Zhang, J. Li, W. Li, X. Zheng, W. Yan, W. Zhang, J. Zhu, R. Si, J. Zeng, *Nat. Commun.* **2019**, *10*, 1885.
- [43] L. Geng, S. Wu, Y. Zou, M. Jia, W. Zhang, W. Yan, G. Liu, *J. Colloid Interface Sci.* **2014**, *421*, 71–77.
- [44] H. Li, L. Wang, Y. Dai, Z. Pu, Z. Lao, Y. Chen, M. Wang, X. Zheng, J. Zhu, W. Zhang, R. Si, C. Ma, J. Zeng, *Nat. Nanotechnol.* **2018**, *13*, 411–417.
- [45] S. Kohl, A. Drochner, H. Vogel, *Catal. Today* **2010**, *150*, 67–70.
- [46] W. Zhan, J. Wang, H. Wang, J. Zhang, X. Liu, P. Zhang, M. Chi, Y. Guo, Y. Guo, G. Lu, S. Sun, S. Dai, H. Zhu, *J. Am. Chem. Soc.* **2017**, *139*, 8846–8854.
- [47] A. Dannenberg, M. E. Gruner, A. Hucht, P. Entel, *Phys. Rev. B* **2009**, *80*, 245438.
- [48] M. Shao, A. Peles, K. Shoemaker, *Nano Lett.* **2011**, *11*, 3714–3719.

Manuscript received: January 2, 2020
Revised manuscript received: March 8, 2020
Accepted manuscript online: April 7, 2020
Version of record online: ■ ■ ■ ■ ■ ■ ■ ■ ■ ■

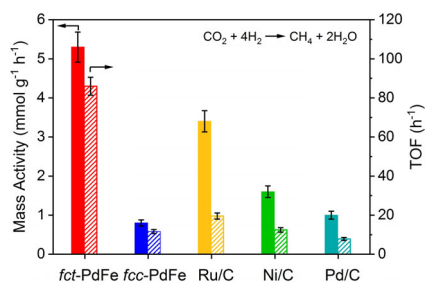
Research Articles



Heterogeneous Catalysis

L. Luo, M. Wang, Y. Cui, Z. Chen, J. Wu,
Y. Cao, J. Luo, Y. Dai, W.-X. Li, J. Bao,*
J. Zeng*

Surface Iron Species in Palladium–Iron
Intermetallic Nanocrystals that Promote
and Stabilize CO₂ Methanation



Intermetallic PdFe nanocrystals afforded high activity and stability for CO₂ methanation. Further mechanistic studies revealed that PdFe intermetallic nanocrystals enabled the maintenance of metallic Fe species via a reversible oxidation–reduction process.

